Analysis of Z-Invariant and Z-Variant Semiconductor Rib Waveguides by Explicit Finite Difference Beam Propagation Method with Nonuniform Mesh Configuration

Youngchul Chung and Nadir Dagli, *Member, IEEE*

Abstract—**An efficient and simple explicit finite difference beam propagation method (EFD-BPM) incorporating nonuniform mesh is described. The criteria for stability is developed and it is shown that this algorithm is power conserving when the stability criteria is met. EFD-BPM is applied to the analysis of single and coupled semiconductor rib waveguides and its accuracy is confirmed by comparing the results with the reported results. Nonuniform mesh is found to improve the efficiency of the method significantly for the analysis of weakly guiding waveguide structures. Several coupled rib waveguide structures with curved input and output branching sections are also analyzed using both three-dimensional EFD-BPM and two-dimensional finite difference BPM combined with effective index approximation and the validity of the latter approach for the analysis of z-variant weakly guiding structures is studied. Zero-gap couplers with deeply etched GaAs rib waveguides are also fabricated and characterized. The experimental results are in good agreement with the theoretical calculations based on EFD-BPM with nonuniform mesh.**

I. Introduction

THE reliable and economically feasible utilization of optical systems based on semiconductor lasers and optical fibers for communication and instrumentation applications require the realization of photonic integrated circuits (PIC). Such circuits use guided optical waves to perform various different functions such as switching, multiplexing, modulation, demodulation, and analog to digital (A–D) conversion. Today there is a significant effort to develop methods to fabricate, design, and analyze PIC. The most basic building block of PIC is the optical waveguide. Of various types of optical waveguides, rib waveguides seem to be the most attractive waveguides for waveguiding in compound semiconductors, which are the most desirable materials for PIC. The refractive index profile of rib waveguides can be controlled and engineered precisely. In addition to the accurate control of the physical properties of the rib waveguides, their accurate and efficient analysis and design are also essential. Such analysis and design methods will eventually generate the computer aided design tools for PIC. So far various different methods have been developed and applied to the analysis of rib waveguides. All these methods can be combined under two groups. One particular group is most suited to the analysis of the waveguides whose cross-sectional dimensions and index profiles do not vary along the direction of propagation. In this work such waveguides are called z-invariant waveguides. The simplest method to analyze z-invariant rib waveguides is the so-called effective index method [1]. This method is only valid for weakly guiding shallowly etched rib waveguides. However, it can still be used to design single-mode, strongly guiding, deeply etched rib waveguides because the propagation constant values that the effective index method predicts are always higher than the actual values [2]. Therefore, the cutoff width values predicted by this method are conservative estimates. On the other hand this method is not applicable to all possible structures and when applicable its accuracy degrades rapidly as the confinement of the mode increases, hence there is a need for efficient numerical methods. For this purpose a finite difference method and variational methods based on Rayleigh–Ritz procedure were developed and their accuracy and computational complexity were compared including the effective index method in this comparison [3]. Finite element methods have also been applied to optical waveguide analysis [4]. Another recently developed method of analysis converts a given optical structure into a modular microwave equivalent circuit [5]. Almost all the other methods to analyze z-invariant waveguides are compared by the working group I of COST 216 project [6].

For the other group of waveguides cross-sectional dimensions and index profiles vary along the direction of propagation. In this paper, such waveguides are called z-variant waveguides. Z-variant waveguides arise both out of practical needs, such as the need to separate the input and output ports of a directional coupler and arms of a Mach–Zehnder interferometer, and out of the desirable features of certain structures such as Y-junction and X-crossing waveguides. The most commonly used method to analyze such structures is the so-called beam propaga-

Manuscript received October 12, 1990; revised May 23, 1991. This work was supported by a UC Micro/Tektronix Grant and by DARPA through the Optoelectronic Technology Center (OTC).

The authors are with the Department of Electrical and Computer Engineering, University of California, Santa Barbara, CA 93106.

IEEE Log Number 9102791.

0018-9197/91$01.00 © 1991 IEEE

tion method (BPM) which is also applicable to the analysis of z-invariant waveguides [7]. Conventional BPM requires fast Fourier transform (FFT) at every propagation step and will be called FFT-BPM in this paper from now on. FFT-BPM is usually combined with the effective index method to convert a three-dimensional structure to an equivalent two-dimensional geometry [8]. It is, of course, also possible to apply FFT-BPM to the analysis of a three-dimensional waveguide geometry [9]. Recently new three-dimensional BPM algorithms were applied to the analysis of single, coupled, and Y-junction rib semiconductor waveguides [10]–[14]. In [10], the propagation constants and mode profiles of the lowest order rib waveguide were calculated utilizing propagation in imaginary z axis. Three-dimensional BPM was also applied to evaluate the radiation loss of rib waveguide Y junctions [10]–[13] and to determine the mode indexes of single waveguides and the even and odd mode indexes as well as coupling lengths of coupled waveguides [14] analyzed in [3].

The analysis of rib waveguides with the FFT-BPM creates a special challenge. The rapid refractive index variations in the rib waveguide cross-sectional profile necessitates the use of large spectral components of the optical field, which in turn forces one to use very small propagating steps [15], [16]. Therefore, even though one can accurately analyze the rib waveguides using FFT-BPM, the need to use very small propagating steps results in exceedingly large computing times. This problem has been recognized and there has been considerable recent research activity to improve the computational efficiency of the FFT-BPM. In one approach finite difference techniques were used to approximate the plane wave propagation operator resulting in more efficient BPM algorithms [11]–[13]. In all these algorithms including FFT-BPM, the exact formal propagation operator is split into several operators, each of which can be easily implemented into a numerical procedure. To keep the error associated with this operator splitting the propagation step lengths should be small. One of the operators, which describes plane wave propagation in a homogeneous medium, can be realized using FFT algorithm, split-step implicit finite difference procedure, and the so-called real-space algorithm. In FFT algorithm, each plane wave component of the field profile is calculated using FFT. Then each plane wave component is propagated in the homogeneous medium, and at the end of the propagation step the field in the real space is calculated using inverse FFT [7], [13]. In split-step finite difference procedure, the field propagation in the x direction is first considered, keeping the y coordinate constant. This makes it possible to use the Crank–Nicholson algorithm resulting in tridiagonal linear equations which can be solved very efficiently. Next the field propagation in the y direction is calculated keeping the x coordinate constant and using the same procedure [11], [13]. In the so-called real-space algorithm, the propagation in the x direction is calculated by multiplying a field column vector at each constant y position with a series of unitary block diagonal matrices. These matrices result from the further splitting of the propagation operator in the x direction. Next the propagation in the y direction is calculated similarly [12], [13]. All the mentioned algorithms are unitary. The real-space and FFT algorithms result in explicit methods, but the computation time in the method based on real space algorithm is far less than that based on FFT algorithm.

In another approach finite difference techniques are directly applied to the paraxial wave equation resulting in finite difference BPM [17], [18], where operator algorithms, hence operator splitting is not used. If one considers only a two-dimensional geometry, then inherently stable and unitary Crank–Nicholson finite difference techniques can be used resulting in a very efficient, stable, and power-conserving algorithm [17]. On the other hand for a three-dimensional geometry, although the same finite difference techniques can still be used, the need to invert a large matrix at every propagation step makes such algorithms unattractive. One can circumvent this difficulty using an explicit finite difference algorithm in the solution of the paraxial wave equation resulting in the so-called explicit finite difference BPM(EFD-BPM). A brief outline of this technique and its application to semiconductor rib Y-junction analysis was given in a recent rapid communication [18]. In this communication, the results obtained using the present scheme are compared with that obtained using the real-space method [12] and it was confirmed that the agreement of both results is very good when the same propagation step size of $\Delta z = 0.01\ \mu$m is used. Both methods are explicit. The EFD-BPM is based on direct approximation of partial derivatives and requires small propagation step size for the stability and power conservation. The real-space method is based on operator splitting and also requires small propagation step size to assure the accuracy. A close observation of these two methods reveals that the number of operations, such as multiplications, additions, etc., required to propagate the beam over a propagation step is less in the EFD-BPM compared to the real-space method. Hence, EFD-BPM consumes less CPU time per propagation step than the real-space method. However, this doesn't necessarily mean that the present scheme is always superior to the real-space method, because the present algorithm requires smaller propagation step size as the mesh size decreases while the so-called real-space method doesn't due to its inherent unitarity. The more detailed comparison of the two different algorithms asks for further study.

In this paper, EFD-BPM incorporating a nonuniform mesh is formulated, the condition for its stability and power conservation is derived, and is applied to analyze several z-invariant and z-variant rib waveguide structures. In Section II, the EFD-BPM using a nonuniform mesh and the condition for its stability and power conservation are given. Next, EFD-BPM is applied to analyze several z-invariant rib waveguide structures analyzed by other researchers to assess its accuracy. In Section IV, EFD-BPM is used to analyze z-variant directional couplers and the results of this analysis are compared with those obtained

from a two-dimensional finite difference BPM combined with effective index approximation. In Section V, the experimental results on zero-gap couplers composed of deeply etched GaAs rib waveguides with large mode size are described. The experimental results are also compared with the theoretical predictions of EFD-BPM with nonuniform mesh. Finally, general conclusions are drawn.

II. Formulation of the Explicit Finite Difference Beam Propagation Method (EFD-BPM)

The paraxial wave equation for main polarization component of the electric field E is as follows.

$$2jk_0 n_r \frac{\partial E}{\partial z} = \frac{\partial^2 E}{\partial x^2} + \frac{\partial^2 E}{\partial y^2} + k_0^2(n^2(x, y, z) - n_r^2)E \tag{1a}$$

where n_r is the reference refractive index and k_0 is the wave vector in the vacuum. An explicit finite difference algorithm can be obtained by directly applying finite difference approximation to (1a). It can be readily seen that the approximation of $\partial E/\partial z$ by forward difference, i.e., $(E(z + \Delta z) - E(z))/\Delta z$, results in an inherent instability for any Δz. However, the explicit algorithm is found to become stable for moderately small Δz, if an alternative and second-order accurate center difference approximation of $\partial E/\partial z$, i.e., $(E(z + \Delta z) - E(z - \Delta z))/2\Delta z$, is used. Then, (1a) can be written as

$$E(z + \Delta z) = E(z - \Delta z) + \frac{\Delta z}{jk_0 n_r} FE(z) \tag{1b}$$

where

$$F = \frac{\partial^2}{\partial x^2} + \frac{\partial^2}{\partial y^2} + k_0^2(n^2(x, y, z) - n_r^2)$$

is a linear operator. The criteria for stability and power conservation of this algorithm will be discussed later in this section. Replacing the derivatives in the linear operator F by finite difference approximations, the paraxial wave equation can be approximated as an explicit finite difference equation with nonuniform mesh size, which is

$$\begin{aligned} E_{pq}(z + \Delta z) = {} & E_{pq}(z - \Delta z) + a_p^- E_{(p-1)q}(z) \\ & + a_p^+ E_{(p+1)q}(z) + c_q^- E_{p(q-1)}(z) \\ & + c_q^+ E_{p(q+1)}(z) + b_{pq}(z) E_{pq}(z) \end{aligned} \tag{2}$$

where

$$a_p^- = \frac{2\Delta z}{jk_0 n_r \, \Delta x_{p-1}(\Delta x_{p-1} + \Delta x_p)} \tag{2a}$$

$$a_p^+ = \frac{2\Delta z}{jk_0 n_r \, \Delta x_p(\Delta x_{p-1} + \Delta x_p)} \tag{2b}$$

$$c_q^- = \frac{2\Delta z}{jk_0 n_r \, \Delta y_{q-1}(\Delta y_{q-1} + \Delta y_q)} \tag{2c}$$

$$c_q^+ = \frac{2\Delta z}{jk_0 n_r \, \Delta y_q(\Delta y_{q-1} + \Delta y_q)} \tag{2d}$$

$$b_{pq}(z) = -a_p^- - a_p^+ - c_q^- - c_q^+ - j\frac{k_0 \Delta z}{n_r}(n_{pq}^2(z) - n_r^2). \tag{2e}$$

In (2), $E_{pq}(z)$ and $n_{pq}(z)$ are the optical field values and the sampled refractive index values, respectively, at $x = x_p$, $y = y_q$ in the computational window, and $\Delta x_p = x_p - x_{p-1}$ and $\Delta y_q = y_q - y_{q-1}$. The optical field distributions at every propagating step can be found by multiplying the optical field column vector $\boldsymbol{E}$ by a very sparse matrix which has only five elements in a row. This fact makes this algorithm much more efficient than the conventional FFT-BPM which requires a fast Fourier transformation at every propagation step rather than a sparse matrix multiplication. For example, in case of 64 × 64 grid points in the computational window, the CPU time per propagation step for the present technique is about 0.2 s/step, whereas CPU time for FFT-BPM is about 3 s/step on a SUN SPARC workstation. As the number of grid points increases, the CPU time for FFT-BPM increases faster than the present technique, and more than an order of magnitude improvement in CPU time per propagation step is commonly achieved. It is also noted that the nonuniform mesh can be used in the present algorithm very easily whereas it cannot be used in the FFT-BPM, which further improves the computational efficiency. On the other hand in the present algorithm, we need to know field distributions at the initial two steps. To calculate the field distributions at the second step given the initial field distribution, we may use a forward finite difference approximation which results in an algorithm similar to (2), where only the electric field distribution at the present step is required to calculate the field at the next step. This procedure is programmed and is confirmed to be stable if one continues to use the algorithm represented by (2) right after the second step. Another approach could be to use the FFT-BPM at the very first propagation step, but this is not appropriate in nonuniform mesh configuration. Once the field values at initial two steps are obtained EFD-BPM can be used to propagate the beam further.

To analyze the stability and power conservation condition, we rewrite the algorithm given by (2) in the following matrix form:

$$\boldsymbol{E}(z + \Delta z) = \boldsymbol{E}(z - \Delta z) + \frac{\Delta z}{jk_0 n_r} \boldsymbol{A}\boldsymbol{E}(z). \tag{3}$$

When the number of mesh points in the x and y directions are N_x and N_y, respectively, the kth component of the column vector $\mathbf{E}(z)$ is the optical field value at $x = x_p$, $y = y_q$, i.e., $E_{pq}(z)$, where q is an integer which doesn't exceed k/N_x and $p = k - qN_x$. The matrix $\mathbf{A}$ is a very sparse matrix whose nonzero components are given by

$$A_{k,k-1} = \frac{2\Delta z}{\Delta x_{p-1}(\Delta x_{p-1} + \Delta x_p)} \qquad \text{for } k \neq qN_x$$

$$A_{k,k+1} = \frac{2\Delta z}{\Delta x_p(\Delta x_{p-1} + \Delta x_p)} \quad \text{for } k \neq qN_x - 1$$

$$A_{k,k+N_x} = \frac{2\Delta z}{\Delta y_{q-1}(\Delta y_{q-1} + \Delta y_q)} \quad \text{for } k < (N_x - 1)N_y$$

$$A_{k,k-N_x} = \frac{2\Delta z}{\Delta y_{q-1}(\Delta y_{q-1} + \Delta y_q)} \quad \text{for } k > N_x - 1$$

$$A_{k,k} = -A_{k,k-1} - A_{k,k+1} - A_{k,k+N_x} - A_{k,k-N_x} + k_0^2(n_{pq}^2(z) - n_r^2).$$

The eigenvalues and eigenvectors of the matrix $\boldsymbol{A}$ are $2k_0n_r\beta_n$ and $\boldsymbol{e}_n$, that is,

$$\boldsymbol{A}\boldsymbol{e}_n = 2k_0n_r\beta_n\boldsymbol{e}_n. \tag{4}$$

The matrix $\boldsymbol{A}$ is not symmetric for nonuniform configuration, but it can be symmetrized if it is multiplied by a diagonal matrix $\boldsymbol{D}^2$ whose components are [21]

$$D_{kk}^2 = (\Delta x_{p-1} + \Delta x_p)(\Delta y_{q-1} + \Delta y_q). \tag{5}$$

Multiplying (4) by $\boldsymbol{D}^2$ and manipulating further one obtains a transformed eigenvalue equation, which is

$$\boldsymbol{S}\boldsymbol{e}_n' = 2k_0n_r\beta_n\boldsymbol{e}_n' \tag{6}$$

where

$$\boldsymbol{S} = \boldsymbol{D}^{-1}\boldsymbol{D}^2\boldsymbol{A}\boldsymbol{D}^{-1} \tag{6a}$$

$$\boldsymbol{e}_n' = \boldsymbol{D}\boldsymbol{e}_n. \tag{6b}$$

The transformed matrix $\boldsymbol{S}$ is symmetric because $\boldsymbol{D}^2\boldsymbol{A}$ is symmetric. Hence, the eigenvalues of $\boldsymbol{S}$, which are $2k_0n_r\beta_n$, are always real and the transformed eigenvectors $\boldsymbol{e}_n'$ form an orthogonal basis set. In the following discussion, $\boldsymbol{e}_n'$'s are assumed to be normalized, hence they form an orthonormal basis set. Furthermore, matrices $\boldsymbol{A}$ and $\boldsymbol{S}$ have the same eigenvalues because they are related to one another through a similarity transformation. The beam propagation algorithm described by (3) can be cast into an equivalent transformed equation, which is

$$\boldsymbol{E}'(z + \Delta z) = \boldsymbol{E}'(z - \Delta z) + \frac{\Delta z}{jk_0n_r}\boldsymbol{S}\boldsymbol{E}'(z) \tag{7}$$

where the $\boldsymbol{E}' = \boldsymbol{D}\boldsymbol{E}$ and the matrix $\boldsymbol{S}$ is given by (6a). The transformed field distribution $E'(z)$ can always be represented by a linear superposition of eigenvectors $\boldsymbol{e}_n'$, which is

$$\boldsymbol{E}'(z) = \sum_n a_n(z)\boldsymbol{e}_n'. \tag{8}$$

Substituting (8) into (7) and multiplying the resulting equation by $\boldsymbol{e}_n'^{*T}$, we can get the difference equation for the unknown amplitude coefficients a_n, which is

$$a_n(z + \Delta z) = a_n(z - \Delta z) + \frac{\Delta z}{jk_0n_r}(2k_0n_r\beta_n)a_n(z). \tag{9}$$

Then we look for the solution of the form

$$a_n(z) = A_n\xi_n^{z/\Delta z} \tag{10}$$

and obtain a quadratic equation for ξ_n, which is

$$\xi_n^2 + j(2\Delta z\beta_n)\xi_n - 1 = 0. \tag{11}$$

The solution of the above quadratic equation for ξ_n is

$$\xi_n = -j\Delta z\beta_n \pm \sqrt{-(\Delta z\beta_n)^2 + 1}. \tag{12}$$

It is readily seen that the magnitude of ξ_n is always unity if we have the condition

$$|\Delta z\beta_n| < 1. \tag{13}$$

To satisfy this condition for every eigenvalue of $\boldsymbol{S}$, Δz should satisfy the following condition

$$\Delta z < \frac{1}{|\beta_n|_{\max}} \tag{14}$$

where $|\beta_n|_{\max}$ is proportional to the eigenvalue of A with the largest magnitude. We can find an upper bound for $|\beta_n|$ using the Gerschgorin's first theorem [22] which states that the magnitude of the eigenvalue of the matrix $\boldsymbol{A}$, $|2k_0n_r\beta_n|$, is always smaller than the largest sum of the absolute values of the elements along any row of the matrix $\boldsymbol{A}$. Hence

$$|2k_0n_r\beta_n| < \frac{4}{\Delta x_{\min}^2} + \frac{4}{\Delta y_{\min}^2} + k_0^2|n_{pq}^2 - n_r^2|_{\max}. \tag{15}$$

Combining (14) and (15) one obtains

$$\Delta z < \frac{1}{|\beta_n|_{\max}} = 2k_0n_r\left\{\frac{4}{\Delta x_{\min}^2} + \frac{4}{\Delta y_{\min}^2} + k_0^2|n_{pq}^2 - n_r^2|_{\max}\right\}^{-1}. \tag{16}$$

When the condition (16) is satisfied, the amplitude coefficient $a_n(z)$ of the transformed eigenvector $\boldsymbol{e}_n'$ is maintained to be constant, i.e., independent of z so that the inner product $\boldsymbol{E}'^{*T}\boldsymbol{E}' = \Sigma_n |a_n(z)|^2$ is constant, hence is conserved. In fact, $\boldsymbol{E}'^{*T}\boldsymbol{E}'$ is the integration of the squared optical field magnitude in the nonuniform mesh configuration. This shows that the condition (16) assures both the stability and the power conservation. The power conservation has been observed in the real computations as long as the stability condition (16) is satisfied. As a power conservation test an eigenmode of a z-invariant waveguide is launched and propagated over a distance of 1 cm in the various computational configurations. At the end of propagation both the power and the shape of the mode were unchanged when the stability condition is satisfied. If the typical rib waveguide parameters ($n_r = 3.34$, $n_{pq} = 1$) for the semiconductor rib waveguides are substituted and $\Delta x_{\min} = \Delta y_{\min} = 0.0625$ μm are used, then Δz should be smaller than 0.014 μm for $\lambda = 1.3$ μm. As Δx and Δy increases, the larger Δz can be allowed. At first such small step sizes may seem to suggest large computational times. Indeed the Δz value required for stability is at the same order of magnitude for the convergence of

conventional BPM. Therefore the number of steps required to propagate the beam remains about the same for both methods. However, the computational effort required to propagate the beam at every step is drastically lower for EFD-BPM since propagation simply requires a sparse matrix multiplication as opposed to fast Fourier transform. As documented earlier in this section, CPU time improvement more than an order of magnitude per propagation step is commonly achieved. Hence even though about the same number of steps is required to propagate the beam over a given distance for both EFD-BPM and FFT-BPM, the overall computational efficiency of EFD-BPM is typically an order of magnitude better than FFT-BPM.

III. Analysis of Z-Invariant Waveguides

The first step to check the accuracy of the present algorithm is to analyze the z-invariant single and coupled waveguides analyzed by different researchers and to compare the results with the reported results. Two methods exist to calculate the propagation constants using BPM's. One method uses the peak position in the power spectra, which is obtained by correlating the propagating fields with the initial field, to obtain the propagation constant of a particular mode [7], [19]. The other method propagates the optical field along imaginary z axis and obtains the modal properties [10]. In this paper, the method described in [7] and [19] is adopted to calculate the propagation constants and coupling lengths.

A. Calculation of Propagation Constants from a Beam Propagation Solution

The field distribution $E(x, y, z)$ everywhere in the z-invariant waveguide can be calculated by applying the algorithms represented by (2). In the course of propagating beam calculation, one calculates the correlation function, which is

$$P(z) = \int\int E^*(x, y, 0)E(x, y, z)\, dx\, dy. \tag{17}$$

On the other hand, $E(x, y, z)$ can be represented by the superposition of orthogonal eigenfunctions of the z-invariant waveguide, which is

$$E(x, y, z) = \sum_n B_n u_n(x, y) \exp(-j\beta_{pn} z) \tag{18}$$

where $u_n(x, y)$ and β_{pn} are the eigenfunction and the propagation constant of the nth rib mode as obtained from the paraxial wave equation. In this expansion it is assumed that degeneracy does not exist, which is a good approximation for rib waveguides. If (18) is substituted into (17), one obtains

$$P(z) = \sum_n |B_n|^2 \exp(-j\beta_{pn} z). \tag{19}$$

The Fourier transform of (19) is

$$P(\beta) = \sum_n |B_n|^2 \delta(\beta - \beta_{pn}). \tag{20}$$

Thus, one can find the propagation constant β_{pn} by numerically calculating the correlation function $P(z)$, Fourier transforming it, and locating the peak in the Fourier domain. Ideally the accurate determination of β_{pn} can only be done by infinitely propagating the beam or when E field value is known over all z because only when z extends to infinity the Fourier transform of (19) will yield (20). However, in practice, one can propagate a beam only a finite length, hence field values over a certain z range, or z window, are known. In mathematical terms this is equivalent to multiplying (17) with a window function $w(z)$, which accounts for the finite length of propagation. Then the Fourier transform of the correlation function, $P_w(z)$, becomes

$$P_w(\beta) = \sum_n |B_n|^2 L(\beta - \beta_{pn}) \tag{21}$$

where the line shape function for the propagation distance D is defined by

$$L(\beta - \beta_{pn}) = \frac{1}{D} \int_0^D \exp[j(\beta - \beta_{pn})z] w(z)\, dz. \tag{22}$$

Knowing this line shape function the propagation constant can be quite accurately determined from the spectrum $P_w(\beta)$ using curve fitting. In the calculations the Hanning window function, $w(z) = 1 - \cos[(2\pi z)/D]$, is used as is typically done in the literature. The eigenfunction of the paraxial wave equation (1a) is identical to that of the original scalar Helmholtz equation. However, the propagation constant of the Helmholtz equation β_h is found from that of the paraxial equation β_p using the relation

$$\beta_h = k_0 n_r (1 + 2\beta_p / k_0 n_r)^{1/2}. \tag{23}$$

The details of calculating the peak position from the spectrum are described in [7] and [19].

B. Calculation of Eigenmode Profile from a Beam Propagation Solution

If both sides of (18) are multiplied by $D^{-1} w(z) \exp(j\beta z)$ and integrated from 0 to D, we can obtain

$$E(x, y, \beta) = \frac{1}{D} \int_0^D E(x, y, z) \exp(j\beta z) w(z)\, dz \tag{24a}$$

$$= \sum_n B_n u_n(x, y) L(\beta - \beta_{pn}). \tag{24b}$$

Thus, for $\beta = \beta_{pi}$, $E(x, y, \beta_{pi})$ can be expressed as

$$E(x, y, \beta_{pi}) = B_i u_i(x, y) L(0) + \sum_{n \neq i} B_n u_n(x, y) L(\beta_{pi} - \beta_{pn}). \tag{25}$$

Equation (25) shows that the eigenmode profile $u_i(x, y)$ can be determined by evaluating the integral (24a) with $\beta = \beta_{pi}$ provided that most of the excited power belongs to the ith mode which is the mode of interest. In practice, such excitation can be achieved in most cases for rib waveguides. The detailed description of this method can be found in [20].

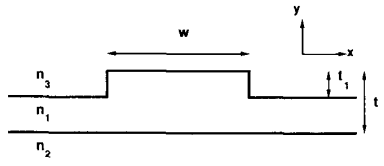

Structure	n_1	n_2	n_3	t [μm]	t_1 [μm]	w [μm]
1	3.44	3.34	1	1.3	1.1	2
2	3.44	3.36	1	1.0	0.1	3
3	3.44	3.435	1	6.0	2.5	4

Fig. 1. Cross-sectional profiles and structural parameters of semiconductor rib waveguide structures that are analyzed in this work.

C. Analysis of z-invariant Waveguide Geometries

In the calculations three different rib waveguides shown in Fig. 1 are considered. The operating wavelength is 1.55 μm. For structure 1 guiding is strong, hence a small computational window size and a uniform mesh configuration is enough for its analysis. Thus, 8 μm × 4 μm window size with 64 and 64 uniform mesh points in x and y directions, respectively, is used to analyze structure 1. For structure 3, however, guiding is very weak both in the vertical and horizontal directions. Thus, a large computational window is required, hence a nonuniform mesh configuration is very useful to reduce the computational time. For the analysis of structure 3, a 130 μm × 33 μm computational window in x and y directions, respectively, is used. In the x direction, the window is partitioned into 3 intervals, where the center 8 μm interval consists of 64 mesh points and the two 61 μm side intervals consist of 64 mesh points each. In the y direction, the window is partitioned into 2 intervals, where the 20 μm substrate interval consists of 20 mesh points and the 13 μm interval above the substrate consists of 108 mesh points. For the analysis of structure 2, a 33 μm × 4 μm window with 512 and 64 uniform mesh points in the x and y directions is used. Table I shows the calculated effective indexes as well as those given in [3], [10], and [14]. The results show that EFD-BPM with uniform or nonuniform mesh configuration is as accurate as the other methods. The computational efficiency of EFD-BPM is at least an order of magnitude better than that of FFT-BPM for all the cases considered. As an illustration of power spectrum from which propagation constant of the paraxial wave equation is calculated, the power spectrum for structure 3 is shown in Fig. 2. A peak is observed representing the guided mode as well as a small amount of power in the radiation modes. The position of the peak can be quite accurately determined by the line fitting method described in [7] and [19]. The mode shape of each single waveguide is found using the method mentioned above and described in [20]. These shapes are found to be quite similar to those shown in [10].

For further check, the coupling lengths of directional couplers composed of two single waveguides shown in Fig. 1 and with gap of 2 μm are calculated. To calculate the even mode effective indices, a sum of two Gaussians

TABLE I
EFFECTIVE INDEXES OF THE RIB WAVEGUIDES SHOWN IN FIG. 1 AS A RESULT OF VARIOUS DIFFERENT APPROACHES

Structure	Present Work	[3]	[10]	[14]
1	3.3913	0.3908	3.3908	3.3913
2	3.3947	3.3953	3.3948	3.3960
3	3.4369	3.4368	3.4368	3.4365

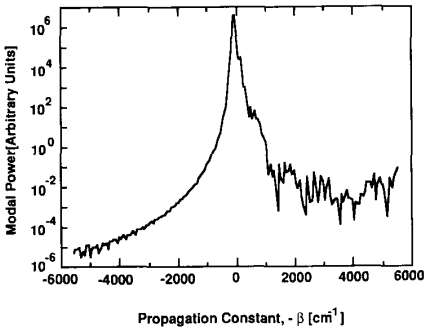

Fig. 2. Modal spectral power of a rib waveguide which is structure 3 in Fig. 1.

TABLE II
COUPLING LENGTHS OF THE DIRECTIONAL COUPLERS COMPOSED OF VARIOUS RIB WAVEGUIDE STRUCTURES SHOWN IN FIG. 1 AS A RESULT OF VARIOUS DIFFERENT APPROACHES

Structure	Present Work	[3]	[14]
1	349 mm	341–357 mm	65.1 mm
2	780 μm	797–827 μm	710 μm
3	–	1273–1968 μm	930 μm

with equal amplitude centered at each arm of directional coupler is excited at the input. For the odd mode calculation, a sum of two Gaussians with equal magnitude and opposite sign is excited at the input so that a sharp peak will occur at the odd mode position in the power spectrum. Table II shows the calculated coupling lengths of directional couplers. For structures 1 and 2, the results are close to the previous results, especially to the results given in [3]. However, there is an uncertainty in accurately locating the odd mode effective index position of structure 3 in the power spectrum. Although in the power spectrum there existed a peak, it was not sharply defined and was intermixed with quasi-continuum. As a refining process, the odd mode index was calculated by using this spectra and the mode profile corresponding to this approximate odd mode index is calculated. This is thought to be a better way of approximating the initial field distribution to determine the odd mode of the coupler. Still the power spectrum didn't show a sharp peak without intermixing of continuum modes. Furthermore it is observed that the mode leaked out as it propagated. From this argument, it is suggested that the odd mode for the coupler from structure 3 is not well defined since it is

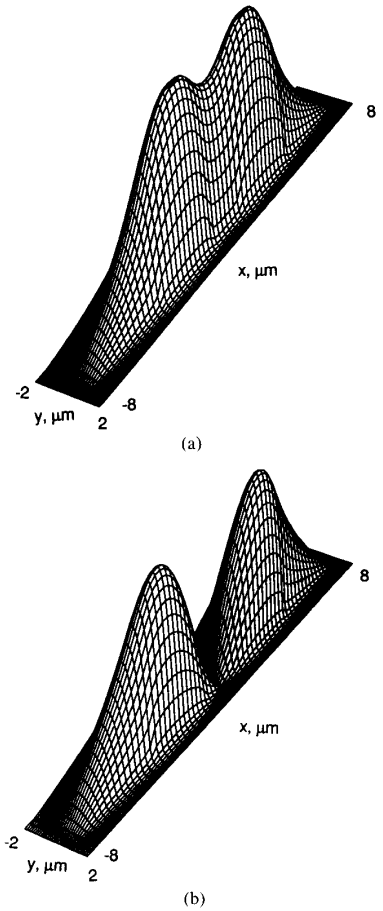

Fig. 3. (a) Even and (b) odd mode profiles of the rib waveguide directional coupler composed of rib waveguides which are the same as structure 2 in Fig. 1.

leaky, hence it is of little meaning to calculate a coupling length for this structure. The same argument has been suggested in [2]. In fact, the calculated coupling length of this coupler varied considerably depending on the methods of calculation employed [2], [3], [14]. For the illustration of the resulting mode profiles, even and odd mode profiles of the coupler composed of structure 2 are shown in Fig. 3.

IV. Analysis of Z-Variant Waveguides with EFD-BPM and Comparison with the Results from Two-Dimensional FD-BPM

The application of EFD-BPM to a strongly guiding *Y*-junction structure and its accuracy and efficiency were recently published [18]. In this section, weakly guiding *z*-variant waveguide structures are analyzed by using both two-dimensional finite difference BPM (FD-BPM) and three-dimensional EFD-BPM. Since the accuracy of EFD-BPM is verified, the applicability of effective index approximation combined with a two-dimensional BPM in the analysis of *z*-variant weakly guiding rib waveguide structures can be assessed.

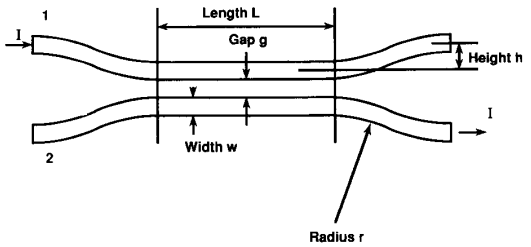

Fig. 4. A rib waveguide directional coupler with curved input and output branching sections. The cross-sectional profile of the rib waveguides is the same as shown in Fig. 1 with $n_1 = 3.23001$, $n_2 = 3.20528$, $n_3 = 1$, $w = 3$ μm, $t = 1.1$ μm, and $t_1 = 0.225$ μm. $h = 25$ μm, $r = 40$ mm.

As an example of a *z*-variant weakly guiding waveguide structure, the couplers with curved branching sections shown in Fig. 4 are considered. These structures are taken from the problem set prepared by the COST-216 working group, which is solved by many different researchers using various different techniques at the 1990 Integrated Photonics Research Conference at Hilton Head, SC. The cross-sectional profile of an individual waveguide is the same as that shown in Fig. 1. The refractive index of the substrate(InP), n_2, is 3.20528, that of the epilayer(InGaAsP), n_1, is 3.23001, and the upper cladding region is air. The width of the individual waveguide w is 3 μm, rib height t is 1.1 μm, and etch depth t_1 is 0.225 μm. The transverse variation of the curved branch h is 25 μm and the radius of curvature r is 40.0 mm.

First, the ratio of the optical power in guide 2 at the output to the total output power as a function of the length of the uniform coupled region L is calculated. At the input guide 1 is excited with its eigenmode. The gap g and the wavelength of operation are 2.5 μm and 1.286 μm, respectively. To get a first approximate solution, a two-dimensional BPM combined with effective index approximation is used. In this approach the three-dimensional index variation is reduced to two-dimensional variation with the help of the effective index approximation and then the two-dimensional FD-BPM is applied. Since the etch depth is not too large, it is expected that this simple approach will give results quite close to those from full three-dimensional analysis. The effective index in the rib region and that outside the rib region are calculated to be 3.21024 and 3.20647, respectively. Then, a two-dimensional FD-BPM, which is proven to be an order of magnitude more efficient than a two-dimensional FFT-BPM [17], is applied to calculate the output power ratio at the end. The size of the computational window is 80 μm with 1024 mesh points. The propagation step size Δz is 5 μm. The three-dimensional EFD-BPM is also applied to analyze these couplers. The computational window size in the x direction is 80 μm with 1024 uniform mesh points. Since the vertical confinement is not so strong, a large vertical computational window size is required to assess the radiation loss properly. The computational window size in the vertical direction is 15 μm. It is partitioned into three regions: a 9.5 μm section with 20 mesh points in the sub-

TABLE III
RATIO OF THE OPTICAL POWER IN GUIDE 2 TO THE TOTAL POWER AT THE OUTPUT FOR DIFFERENT LENGTHS OF THE UNIFORM SECTION OF THE DIRECTIONAL COUPLER STRUCTURE SHOWN IN FIG. 4. AT THE INPUT, GUIDE 1 IS EXCITED WITH THE EIGENMODE OF THE WAVEGUIDE. THE GAP g IS MAINTAINED TO BE 2.5 μm

Length of Uniform Section, L(mm)	Two-Dimensional FD-BPM	Three-Dimensional EFD-BPM
0	0.433	0.453
1	0.757	0.784
2	0.093	0.049
3	0.987	0.988
4	0.012	0.098

TABLE IV
RATIO OF THE OPTICAL POWER IN GUIDE 2 TO THE TOTAL POWER AT THE OUTPUT FOR DIFFERENT GAP SIZES OF THE DIRECTIONAL COUPLER STRUCTURE SHOWN IN FIG. 4. AT THE INPUT, GUIDE 1 IS EXCITED WITH THE EIGENMODE OF THE WAVEGUIDE. THE LENGTH OF THE UNIFORM SECTION L IS MAINTAINED TO BE 2 mm.

Gap, g(μm)	Two-Dimensional FD-BPM	Three-Dimensional EFD-BPM
2.5	0.093	0.050
3	0.304	0.304
3.5	0.841	0.799

strate, a 2.5 μm section with 35 mesh points above it in the region containing the epilayer under the rib, and a 3 μm section above that with 9 mesh points in the air region. For this mesh choice the maximum propagation step size for stability is 0.02 μm. In the calculations propagation step size is chosen as 0.019 μm. It should be noted that this step size is 250 times smaller than the step size used in FD-BPM analysis. The results are summarized in Table III. As can be seen, the effective index approximation and FD-BPM analysis in this case is quite good compared with the full three-dimensional results. The radiation loss due to the branched section is evaluated using both the two-dimensional FD-BPM and three-dimensional EFD-BPM. For the two-dimensional FD-BPM, the excess radiation loss is about 0.04 dB whereas it is about 0.12 dB for the three-dimensional EFD-BPM. This suggests that the two-dimensional FD-BPM tends to give less excess radiation loss than the three-dimensional EFD-BPM even though for both cases the excess loss is very small.

The ratio of optical powers in the guide 2 at the output for g = 2.5, 3, and 3.5 μm when guide 1 is excited with its eigenmode, are also calculated both with the two-dimensional FD-BPM and with the three-dimensional EFD-BPM keeping the length of the uniform region L as 2 mm. The mesh configurations are the same as before. The results are summarized in Table IV. It is noted that the two-dimensional FD-BPM combined with effective index approximation is an efficient and good approximate approach for the analysis of shallowly etched rib waveguide structures.

V. EXPERIMENTAL RESULTS ON DEEPLY ETCHED GaAs RIB WAVEGUIDE ZERO-GAP COUPLERS

The accuracy of any theoretical method should be ultimately compared with the experimental results. For this purpose deeply etched GaAs rib waveguide zero gap couplers are fabricated and characterized. Deeply etched rib waveguides with large mode size are quite attractive because of their compatibility with single-mode optical fibers. However, a fully three-dimensional analysis is inevitably required for the accurate modeling of such guided-wave devices due to deeply etched side walls. The cross-sectional profile of the rib guides together with the nonuniform mesh configuration used in the EFD-BPM analysis and the top view of the zero-gap coupler are shown in Fig. 5. In the experiments only one waveguide width of nominal value 4 μm and several different zero-gap couplers with different uniform region lengths L are used. The nominal width of the uniform zero-gap section was 8 μm. In the fabrication, chemical vapor deposition (CVD) grown undoped GaAs layers on 100 oriented n^+ GaAs substrates were used. The epilayer thickness and the doping levels were 6 μm and 1×10^{16} cm^{-3}, respectively. The substrate doping was specified to be in the low 10^{18} cm^{-3} range. The exact knowledge of the index step between the epilayer and the substrate is crucial to the accuracy of the theoretical analysis. Therefore the index step between the epilayer and the substrate was experimentally measured. For this purpose different slab guides were obtained by etching the epilayer at 1 μm steps and slab guides were tested at 1.15 μm with TE polarization. For this wafer it was found that 4 μm thick slab supported only the fundamental mode while 5 μm and thicker layers supported the first- and second-order modes. The index of the guiding layer, which is undoped GaAs, is 3.45 at 1.15 μm [23]. Knowing this index, the wavelength and the limits on the cutoff thickness of the second slab mode, one can use the well-known slab dispersion relationship to confidently say that the index step is between 4.25×10^{-3} and 6.25×10^{-3}. Thus it is a reasonable choice to take the index step as $(5.25 \pm 1) \times 10^{-3}$.

In the simulations, a nominal value of 5.25×10^{-3} is used. The rib guides were fabricated using reactive ion etching (RIE). As a mask for RIE, a trilevel mask was used. First, a 3000 Å thick PMMA layer was spin coated on the GaAs material and baked. Then a 500 Å thick Ti layer was evaporated on the PMMA layer. This layer is used to prevent the intermixing of PMMA with the photoresist layer used in standard lithography in the next step. Finally using standard lithographic techniques 1000 Å thick Ni waveguide patterns were defined on the Ti layer using lift off. Ni patterns defined this way provide the masking for RIE. After the mask fabrication is complete the patterns were etched 4 μm deep using chlorine based RIE. After the etching was done, the RIE mask was removed by dissolving PMMA in acetone. Due to the limitations of the optical lithography process used, the ends of the curved waveguides, where they are connected with

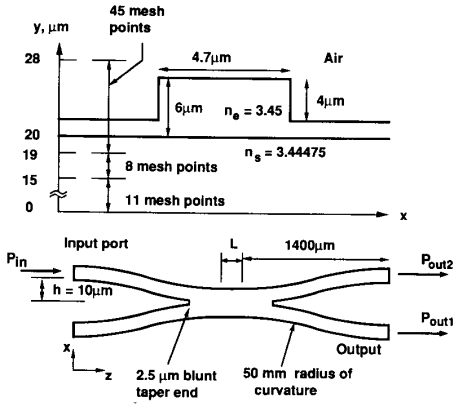

Fig. 5. Cross-sectional profile of the GaAs rib waveguides and schematic top view of the zero-gap couplers used in the experiments. On the cross-sectional profile of the single waveguide the nonuniform mesh configuration in the y direction is also indicated.

the zero-gap coupling region at the center, did not turn out to be smooth and resulted in a 2.5 μm blunt taper end as indicated in Fig. 5. The waveguide width after the etching was measured to be 4.7 μm. The width of the uniform zero-gap section at the center was 9 μm. To assess the radiation loss of the zero-gap couplers straight waveguides were also fabricated beside each zero-gap coupler.

During the optical measurement the output of a 1.15 μm He–Ne laser was endfire coupled into the guides using a microscope objective lens. The near field output pattern was imaged onto a vidicon camera and displayed onto a TV monitor. For fine alignment purposes piezoelectric positioners, which allow a precision less than a micrometer, were used. Fig. 6(a) shows the rib waveguide cross-sectional profile at the output of a zero-gap coupler and the measured and calculated output field profiles for two different lengths of uniform region. The measured and simulated output field profiles show good agreement. The calculated field profile just after the curved output waveguides shows a fair amount of optical intensity outside of the rib waveguides. This is the radiating part of the optical field and is mainly due to blunt taper end. In the experiment, this radiated field profile was not observed because of the presence of 5 mm long straight waveguides between just after the curved waveguides and the cleaved end of the crystal where output profile was measured.

Relative crossover power and transmission are also measured and the results are shown in Fig. 6(b) as a function of the length of the uniform zero-gap section. The relative crossover power is defined as $P_{out1}/(P_{out1} + P_{out2})$. Relative transmission is the ratio of the total output power in guides 1 and 2 to the output power of a straight waveguide next to the zero-gap coupler. The same structures are also simulated with EFD-BPM. During the EFD-BPM simulations, in the x direction, a uniform mesh with 256 points over a 60 μm window was used. In the y direction, a nonuniform mesh shown in Fig. 5 was used. The propagation step size was 0.075 μm and CPU time for propagating the beam over 1 mm was about 80 min on

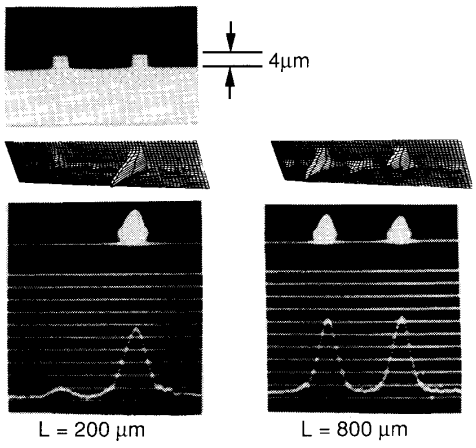

(a)

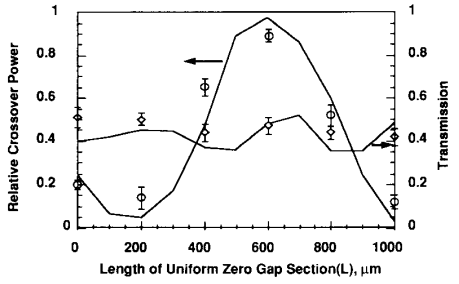

(b)

Fig. 6. (a) The cross-sectional profile of the fabricated rib waveguides at the output of a zero-gap coupler. The measured and simulated output profiles for two different uniform zero-gap section lengths are also shown. (b) The relative crossover power $P_{out1}/(P_{out1} + P_{out2})$ and transmission of zero-gap couplers as a function of uniform zero-gap section length. The continuous curves are the results of the simulations and the data points are the results of the experiments.

a SUN-SPARC workstation and 75 s on a CRAY-2 supercomputer. In the simulations, first the eigenmode of single rib straight waveguide is calculated using the method described in Section III. Then one input arm of the coupler was excited with this eigenmode. The power at each output arm was found by calculating the overlap integral of the resulting field distribution with the eigenmode of the straight waveguide.

Fig. 6(b) shows that experimental and calculated results are in good agreement. The relatively low transmission and its oscillatory behavior are due to blunt taper ends at the input and output. As the length of the uniform zero-gap section L varies the field profile at the blunt taper end at the output also varies. Hence the radiation caused by this blunt taper end also varies resulting in oscillatory transmission behavior. This behavior is also predicted by the simulations.

VI. Conclusion

An efficient and simple three-dimensional explicit finite difference beam propagation method (EFD-BPM) to analyze an arbitrary three-dimensional waveguiding geometry is described. Condition for the stabiliy of EFD-BPM algorithm is derived and it is shown that when stability

condition is met power conversation is assured. Its accuracy is confirmed by analyzing singe and coupled z-invariant rib waveguides and comparing the results with the previously reported results. The EFD-BPM is an order of magnitude faster than the standard BPM employing FFT in advancing the beam over a propagation step. To improve the computational efficiency per propagation step even further, EFD-BPM with nonuniform mesh configuration is developed and applid to the analysis of z-invariant and z-variant structures. It is confirmed that this approach reduces the computation time further by a factor of a few while maintaining the accuracy. However, compared to FFT-BPM the maximum step size for the stability of EFD-BPM is about the same. But due to more than an order of magnitude improvement per propagation step overall computational efficiency of EFD-BPM was found to be at least an order of magnitude better than FFT-BPM. With the help of three-dimensional EFD-BPM the applicability of a two-dimensional finite difference BPM combined with effective index approximation for weakly guiding z-variant structure is also studied and verified. Finally, experiments on GaAs zero-gap couplers with deeply etched rib waveguides are performed and experimental results were found to be in good agreement with the nonuniform mesh EFD-BPM simulations, once again confirming EFD-BPM to be a very accurate and efficient modeling tool for the design and analysis of practical guided-wave devices.

ACKNOWLEDGMENT

The authors thank C. P. Chao and I.-H. Tan for their help on the reactive ion etching.

REFERENCES

[1] R. M. Knox and P. P. Toulios, "Integrated circuits for the millimeter through optical range," in *Proc.*, MRI Symposium on Submillimeter waves. Brooklyn, NY: Polytechnical, 1970, pp. 497-516.

[2] N. Dagli and C. G. Fonstad, "Theoretical and experimental study of the analysis and modeling of integrated optical components," *IEEE J. Quantum. Electron.*, vol. 24, pp. 2215-2226, Nov. 1988.

[3] M. J. Robertson, S. Ritche, and P. Dayan, "Semiconductor waveguide: analysis of optical propagation in single rib structures and directional couplers," *IEE Proc.*, vol. 132, pp. 336-342, 1985.

[4] B. M. A. Rahman and J. B. Davies, "Finite element analysis of optical and microwave waveguide problems," *IEEE Trans. Microwave Theory Tech.*, vol. MTT-32, pp. 20-28, Jan. 1984.

[5] N. Dagli, "Equivalent circuit representation of open guided-wave structures," *IEEE J. Quantum Electron.*, vol. 26, pp. 98-108, Jan. 1990.

[6] Working Group I, COST 216, "Comparison of different modelling techniques for longitudinally invariant integrated optical waveguides," *IEE Proc.*, vol. 136, Pt. J, pp. 273-280, 1989.

[7] M. D. Feit and J. A. Fleck, Jr., "Computation of mode properties in optical fiber waveguides by the propagating beam method," *Appl. Opt.*, vol. 19, no. 7, pp. 1154-1164, 1980.

[8] A. Neyer, W. Mevenkamp, L. Thylen, and B. Lagerstrom, "A beam propagation method analysis of active and passive waveguide crossings," *J. Lightwave Technol.*, vol. LT-3, pp. 635-642, Mar. 1985.

[9] M. D. Feit and J. A. Fleck, Jr., "An analysis of intersecting diffused channel waveguides," *IEEE J. Quantum Electron.*, vol. QE-21, pp. 1799-1805, Nov. 1985.

[10] D. Yevick and B. Hermansson, "New formulation of the beam propagation method: application of rib waveguides," *IEEE J. Quantum Electron.*, vol. 25, pp. 221-229, Feb. 1989.

[11] ——, "Split-step finite difference analysis of rib waveguides," *Elec. Lett.*, vol. 25, no. 7, pp. 461-462, 1989.

[12] D. Yevick and M. Glasner, "Analysis of forward wide-angle light propagation in semiconductor rib waveguides and integrated-optic structures," *Elec. Lett.*, vol. 25, no. 23, pp. 1611-1612, 1989.

[13] D. Yevick and B. Hermansson, "Efficient beam propagation techniques," *IEEE J. Quantum Electron.*, vol. 26, pp. 109-112, Jan. 1990.

[14] M. D. Feit and J. A. Fleck, Jr., "Analysis of rib waveguides and couplers with the propagating beam method," Numer. Simulation and Analysis in Guided-Wave Opt. and Optoelectron. Workshop, vol. 3, pp. 32-35, 1989.

[15] L. Thylen, "The beam propagation method: an analysis of its applicability," *Opt. Quantum Electron.*, vol. 15, no. 5, pp. 433-439, 1983.

[16] J. Van Roy, J. van der Donk, and P. E. Lagasse, "Beam propagation method: analysis and assessment," *J. Opt. Soc. Amer.*, vol. 71, no. 7, pp. 803-810, 1983.

[17] Y. Chung and N. Dagli, "An assessment of finite difference beam propagation method," *IEEE J. Quantum Electron.*, vol. 26, pp. 1335-1339, 1990.

[18] ——, "An explicit finite difference beam propagation method: application to semiconductor rib waveguide Y-junction analysis," *Electron. Let.*, vol. 26, no. 11, pp. 711-713, 1990.

[19] M. D. Feit and J. A. Fleck, Jr., "Mode properties of optical fibers with lossy components by the propagating beam method," *Appl. Opt.*, vol. 20, no. 5, pp. 848-856, 1981.

[20] ——, "Computation of mode eigenfunctions in graded-index optical fibers by the propagating method," *Appl. Opt.*, vol. 19, no. 13, pp. 2240-2246, 1980.

[21] I.-H. Tan, G. L. Snider, L. D. Chang, and E. L. Hu, "A self-consistent solution of Schrodinger–Poisson equations using a nonuniform mesh," *J. Appl. Phys.*, vol. 68, pp. 4071-4076.

[22] G. D. Smith, *Numerical Solution of Partial Differential Equations: Finite Difference Methods*. New York: Oxford Univ. Press, 1985, p. 60.

[23] J. S. Blakemore, "Semiconducting and other major properties of gallium arsenide," *J. Appl. Phys.*, vol. 53, no. 6, pp. R123-R181, 1982.

Youngchul Chung was born in Pusan, Korea, on January 20, 1959. He received the B.S. degree in electronics engineering from Seoul National University, Korea, in 1981, and the M.S. degree in electrical engineering from Korea Advanced Institute of Science and Technology, Seoul, Korea, in 1983. He is currently pursuing the Ph.D. degree in electrical and computer engineering at the University of California, Santa Barbara.

From 1983 to 1986 he was a research engineer with Gold Star Cable Co., Anyang, Korea, working on the design, installation, and management of local area network system. From 1986 to 1988 he was a researcher with the Research Division of Korea Advanced Institute of Science and Technology. He conducted research on the analysis and fabrication of two-mode-interference wavelength division multi-demultiplexer. His current research interests are the design, fabrication, and modeling of passive and active guided-wave devices in III-V compound semiconductors.

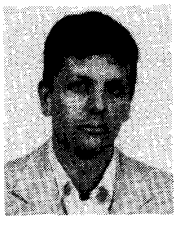

Nadir Dagli (S'77-M'86) was born in Ankara, Turkey. He received the B.S. and M.S. degrees in electrical engineering from Middle East Technical University, Ankara, Turkey, in 1976 and 1979, respectively, and the Ph.D. degree, also in electrical engineering, from the Massachusetts Institute of Technology, Cambridge, in 1986. During his Ph.D. research he worked on the design, fabrication, and modeling of guided-wave integrated optical components in III-V compound semiconductors. He also worked on III-V materials preparation by LPE and the modeling and analysis of heterojunction bipolar transistor for microwave and millimeter-wave applications.

He is currently an Assistant Professor at the University of California, Santa Barbara. His research interests include the design, fabrication, and modeling of guided-wave components for optical integrated circuits, solid-state microwave and millimeter-wave devices, electron waveguides, and novel quantum interference devices.

Dr. Dagli is the recipient of the 1990 UCSB Alumni Association Distinguished Teaching Award.